



High-resolution imaging of the melt distribution in partially molten upper mantle rocks: evidence for wetted two-grain boundaries

G. Garapić

Department of Earth Sciences, Boston University, Boston, Massachusetts, USA (gsiftar@bu.edu)

U. H. Faul

Department of Earth Sciences, Boston University, Boston, Massachusetts, USA

Division of Materials Science and Engineering, Boston University, Boston, Massachusetts, USA

E. Brisson

Scientific Computing and Visualization Group, Boston University, Boston, Massachusetts, USA

[1] We determine the 3-D melt geometry of partially molten samples of olivine containing 1.6 and 3.6 vol.% of basaltic melt that were held in a piston cylinder apparatus at upper mantle conditions for 430 h. Our approach involves serial sectioning and high-resolution field emission SEM imaging. Resolution is such that melt pockets approaching ~30 nm in size were resolved while covering an area of ~300 by 230 μm . The principal result of this study is to show that thin layers (typically 100 nm or less in thickness) between adjacent grains observed in 2-D images persist with depth and are therefore wetted two-grain boundaries. Melt geometries most closely resembling triple junction tubules of the isotropic equilibrium model occur at all three-grain edges but are small compared to larger pockets. The wetted grain boundaries at a dihedral angle $>0^\circ$ for this system are inferred to be due to slow expulsion of melt from dynamically reorganizing grain boundaries during steady state grain growth. The attenuation peak observed in forced torsional oscillation experiments on similar samples is likely related to the wetted grain boundaries. Grain growth, driven by surface energy reduction, occurs also at the larger grain sizes expected for the mantle. This suggests the presence of wetted grain boundaries and significant velocity reduction and attenuation in partially molten upper mantle, as observed for example in back-arc basins.

Components: 6,700 words, 8 figures.

Keywords: melt geometry; asthenosphere; partial melt; olivine; grain growth.

Index Terms: 5112 Physical Properties of Rocks: Microstructure; 5114 Physical Properties of Rocks: Permeability and porosity; 5144 Physical Properties of Rocks: Wave attenuation.

Received 13 November 2012; **Revised** 10 January 2013; **Accepted** 10 January 2013; **Published** XX Month 2013.

Garapić, G., U. H. Faul, and E. Brisson (2013), High-resolution imaging of the melt distribution in partially molten upper mantle rocks: evidence for wetted two-grain boundaries, *Geochem. Geophys. Geosyst.*, 14, doi:10.1029/2012GC004547.

1. Introduction

[2] The dynamics of partially molten regions of the upper mantle is linked to the amount of melt retained in the solid matrix. The retained melt determines the buoyancy and affects the viscosity of the partially molten region [e.g., Šrámek *et al.*, 2007; Hernlund *et al.*, 2008; Katz, 2008, 2010; Simpson *et al.*, 2010; Herbert and Montési, 2010]. The geometry of the retained melt determines the permeability, which in turn affects trace element and U-series isotope geochemistry [e.g., Johnson *et al.*, 1990; Spiegelman and Kenyon, 1992; Stracke *et al.*, 2006]. Moreover, detection of melt by seismic or electromagnetic imaging techniques is sensitive to melt fraction and geometry [e.g., Faul *et al.*, 1994; Takei, 2002; ten Grotenhuis *et al.*, 2005; Yoshino *et al.*, 2010; Watson and Roberts, 2011]. While it is uncontroversial that basaltic melt in an olivine matrix is interconnected at all melt fractions, the melt geometry and hence residual porosity during the melting process is less well agreed upon.

[3] A simplified model of the melt geometry for a two-phase system of olivine and basaltic melt was adapted from early studies in materials science [Waff and Bulau, 1979; Bulau *et al.*, 1979]. The 3-D melt distribution was obtained by computing the geometry of solid-liquid interfaces at three-grain edges and four-grain corners at chemical equilibrium and under hydrostatic conditions [von Barga and Waff, 1986]. The calculations are based on the (local) balance of surface tension between melt and uniformly sized crystalline grains with the assumption of a single-valued dihedral angle θ (implying crystalline isotropy). In this system, melt forms an interconnected network of tubules along three-grain edges for dihedral angles $0^\circ < \theta < 60^\circ$ but does not wet two-grain boundaries. Based on this model, measurement of the dihedral angle from experiments is sufficient to fully characterize the 3-D melt geometry.

[4] Studies on experimentally produced partially molten olivine showed that the melt geometry differs significantly from this ideal model [Waff and Faul, 1992; Faul *et al.*, 1994; Faul, 1997]. Melt is present not only at three-grain edges, in agreement with the idealized model, but also in large pockets surrounded by four or more grains and in thin melt inclusions (layers) connecting neighboring triple junctions. Due to the relatively uniform width and frequent occurrence of the layers, the authors concluded that they represent wetted two-grain boundaries.

[5] Subsequent studies, however, affirmed the self-similar isotropic model. Wark *et al.* [2003] stated

that the thin inclusions were not wetted two-grain boundaries but triple junction tubules sectioned along their long axes. The grain boundary wetness (the fraction of grain boundary length wetted by melt relative to the total grain boundary length in 2-D sections) was found to be in agreement with the predictions of the isotropic model [Yoshino *et al.*, 2005]. A synchrotron X-ray microtomography study [Zhu *et al.*, 2011] of experimental samples yielded 3-D images of the melt geometry that were similarly inferred to be compatible with the isotropic model.

[6] As discussed below, resolution is a key factor for determination of the melt geometry both in two and three dimensions. This study provides a three-dimensional view of the melt geometry in partially molten olivine derived from high-resolution 2-D images. A primary aim is to determine whether the layers observed in these images represent wetted two-grain boundaries.

2. Methods

2.1. Sample Preparation

[7] Samples with two different melt contents were analyzed in this study. The samples consist of solution-gelation derived Fo₉₀ olivine and added basaltic melt (2 wt.%, SB8 and 4 wt.%, SB11, see Faul and Scott [2006]). The samples were run in a piston cylinder at 1350°C and 1 GPa for 432 h, with resulting mean grain sizes of 33 μm . The melt composition was designed to be in equilibrium with a four-phase assemblage (olivine, two pyroxenes, and plagioclase) at 1250°C and 300 MPa. At the temperature of this study, some orthopyroxene (<1%) crystallizes, resulting in melt contents that are slightly below the amount of basalt added (see below). The samples were sectioned longitudinally through the center, vacuum-impregnated in epoxy, polished on successively finer grid size abrasives and finally in suspensions of alumina and colloidal silica on a vibrating polisher. The starting grain size of the synthetic olivine is about 1 μm , so that steady state grain growth conditions prevail after about 2 h at this temperature [Faul and Scott, 2006]. Consequently, the microstructure, including the melt geometry, evolved as a result of steady state grain growth during the experimental run time.

2.2. Serial Sectioning and Image Acquisition

[8] In each serial sectioning step, we polished the samples for 5 h on colloidal alumina to avoid

plucking of the grains and one additional hour on colloidal silica to obtain the highest quality surface for imaging purposes. The imaging was conducted on a Zeiss Supra VP 40 FE-SEM (SB11) and Zeiss Supra VP 55 FE-SEM (SB8) at 10 kV acceleration voltage and 4.3 mm working distance, with an aperture of $30\ \mu\text{m}$. Each image had a size of 2048×1536 pixels with a resolution of $0.026\ \mu\text{m}/\text{pixel}$ at 256 gray scales. Each 2-D section consists of a mosaic of 6×6 overlapping images for a total imaged area of $300 \times 230\ \mu\text{m}$ or 12000×9025 pixels. A total of 24 sections were imaged, resulting in a depth of $38\ \mu\text{m}$ (for a total of 2.6×10^9 pixels).

2.3. Section Thickness Measurements

[9] In order to determine the thickness of the removed material, we drilled two laser holes with a Merchantek LUV213 laser in each sample. Following each polishing step, we measured the depth of the two laser holes with a white light interferometer, Zygo [e.g., *Lamarre et al.*, 2009], which has a relative vertical resolution of $0.01\ \mu\text{m}$. The laser holes, as the only vertical features in samples, were also used for the alignment of the 2-D sections and the reconstruction of the melt geometry. For this purpose, a circle was fitted to the laser holes for each sectioning step, with the coordinates of the circle center as a reference point for vertical alignment.

[10] Figure 1 shows the decrease in depth for the two laser holes versus the section number for sample SB11. Depth decreases equally in both holes, indicating that the sample surface does not become canted during sectioning. The average section thickness can be calculated from the slope of the lines as $1.6\ \mu\text{m}$. However, for the 3-D reconstruction, the measured thickness for each section was used. To improve the depth measurements and vertical alignment, a true UV laser may produce smaller diameter holes with a smoother, more reflective bottom.

2.4. Image Processing, 3-D Reconstruction, and Vertical Resolution

[11] Following image acquisition, the gray-scale images need to be segmented (into melt and solid) in order to convert them to binary images. Because melt (quenched to glass) is softer, it is preferentially removed during the final polishing steps. The resulting topography causes uneven illumination during imaging and consequently nonuniform gray scales of the glass, particularly near grain edges. Conversion to binary images therefore required hand digitization of melt-solid interfaces for further processing with Image J. The mosaics of the binary

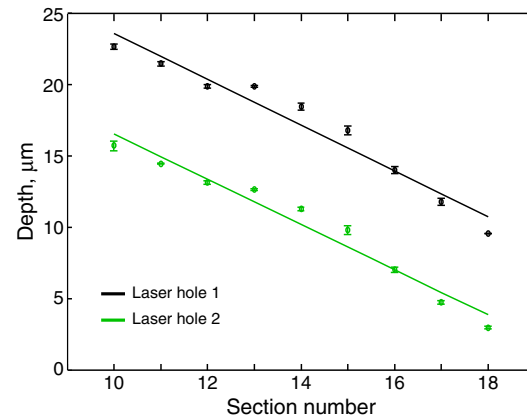


Figure 1. Change in depth of the laser holes with progressive removal of material by polishing. The two holes on either side of the imaged area show consistent depth changes, illustrating that the sectioning process does not result in canting of the sample surface. The average section thickness is $\sim 1.6\ \mu\text{m}$ and the total thickness of the removed material is $\sim 40\ \mu\text{m}$. For 3-D reconstruction the section thickness measured for each slice was used rather than the average.

images of each section were then stacked and aligned using the laser holes as described above.

[12] To construct the 3-D melt surfaces from adjacent horizontal slices for sample SB11, we used a 3-D alpha-shape technique. Loosely speaking, alpha shapes provide us with an effective way to reconstruct a surface at a particular scale of “smoothness,” controlled by the parameter alpha [*Edelsbrunner and Mucke*, 1994]. The parameter alpha can be varied so as to give the desired level of surface detail. For this computation, we used the program CGAL, which outputs the alpha shapes as a triangular mesh for rendering. CGAL was also used to sample the tetrahedral mesh comprising the alpha complex, interpolating between the original sections to produce isometric voxels. These uniform volume data were needed for morphological operations, such as erosion. Autodesk Maya was finally used to render the surface of the 3-D pore space.

3. Results

[13] Figures 2 and 3 show the 2-D microstructures in samples SB11 and SB8, respectively, at a scale and resolution comparable to previously published images [*Faul*, 1997, 2000; *Wark et al.*, 2003; *Yoshino et al.*, 2005; *Faul and Scott*, 2006]. Larger pockets of melt surrounded by more than three grains can easily be identified in these images. At

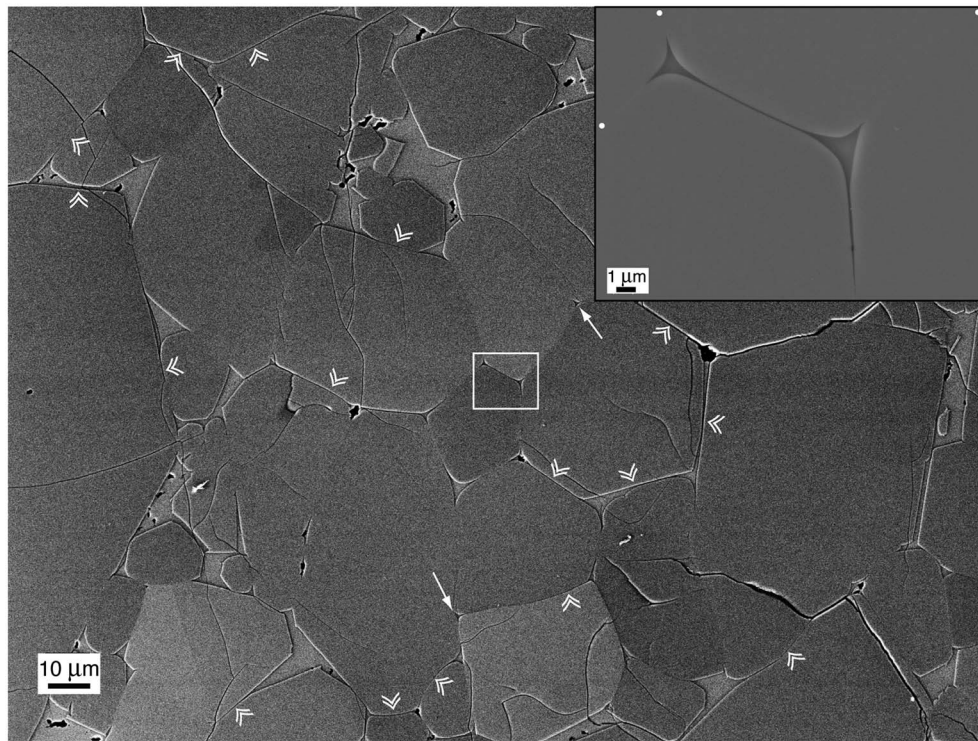


Figure 2. Scanning electron microscope (SEM) image of the melt distribution in sample SB11 with an average melt content of 3.6%. The relatively low-magnification image provides an overview of the microstructure. The different gray scales of olivine grains are due to orientation contrast. Single white arrows point to triple junctions with diameters of 1 μm or less. Double arrow heads point to wetted two-grain boundaries observable at higher resolution. Large melt pockets surrounded by faceted olivine grains are prominent for example near the top of the image. The white rectangles indicate the area shown at high resolution in the inset of two triple junctions connected by a thin layer of melt. Melt extends also onto the grain boundary towards the bottom of the image but does not wet it completely. White dots indicate melt-free grain boundaries which are observable by the orientation contrast in the large image but show no preferential removal of material due to polishing.

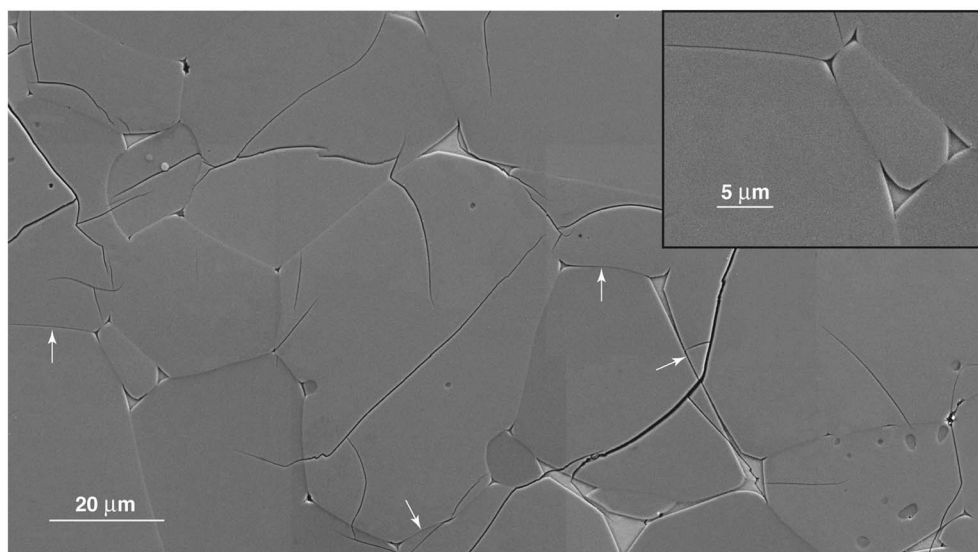


Figure 3. Mosaic of SEM images of the microstructure of sample SB8 with 1.6% melt. As at the higher melt fraction, the melt distribution is not uniform on the grain scale. Melt pockets bounded by more than three grains, often with faceted interfaces, contain most of the melt. Triple junction-like geometries are often 1 μm or less in diameter (see enlarged inset). Wetted grain boundaries (white arrows) occur less frequently than at the higher melt fraction. The layer of melt on the left in the inset is about 50 nm wide.

the lower melt fraction of sample SB8, some areas appear to be melt free (Figure 3), but close inspection shows that all three-grain edges contain melt in both samples. Therefore, the triple junctions form a continuously connected network. However, a number of triple junctions particularly in SB8 are $1\ \mu\text{m}$ or less in diameter.

[14] Thin layers separating neighboring grains with a thickness >20 to $100\ \text{nm}$ can only clearly be seen at the higher resolution in Figures 2 (inset) and 3 (inset). Glassy layers with a thickness in the same range have been reported from transmission electron microscope (TEM) observations of similar samples [Vaughan *et al.*, 1982; Cmiral *et al.*, 1998]. Observation of the layers at the resolution of the FE-SEM imaging used here is aided by the preferential polishing of glass and rounding of adjacent grain edges. Melt-free grain boundaries are not affected by preferential polishing (e.g., Figure 2, inset).

[15] Comparison of Figures 2 and 3 shows that layers occur more frequently in the sample with the higher melt content. The increase in the number of wetted grain boundaries with increasing melt fraction is more obvious in binary images, where the areas representing melt are black (Figure 4). While there are some wetted grain boundaries at the lower melt content of sample SB8, the number is significantly higher at the higher melt content of sample SB11, where the majority of melt pockets are connected in the 2-D section. At the lower melt content, the contrast in size between the triple junctions and larger pockets is particularly evident.

[16] The melt content was determined from binary images such as those shown in Figure 4. The binary images in this figure show a representative section for each sample (Figure 6 shows all sections for SB8). For determination of the grain boundary wetness, the binary images were used together with grain boundary maps. The grain boundary wetness is defined as the solid-liquid boundary area (length) divided by the total grain boundary area (length) [Takei, 1998]. The melt contents of 1.6 and 3.6 vol.% were determined by averaging the values from all sections of each sample (SB8 and SB11, respectively). The corresponding values for the grain boundary wetness are 0.27 and 0.65. For comparison with these relatively coarse-grained samples ($33\ \mu\text{m}$), a fine-grained sample run at the same temperature but for 2 hours only (mean grain size of $8.5\ \mu\text{m}$) with 3.9% melt in the analyzed section has a wetness 0.32. Together, these observations indicate that the grain boundary wetness increases with melt content at fixed grain size, as well as with grain size at (nearly) constant melt content.

[17] Serial sectioning shows that the layers separating neighboring grains can be tracked through the sample (Figure 5). The persistence of the layers with depth over more than $10\ \mu\text{m}$ for larger grains shows that they cannot be triple junctions sectioned parallel to their long axes [cf. Wark *et al.*, 2003], as triple junction tubule-like melt pockets typically are about $1\ \mu\text{m}$ in diameter. The layers identified in 2-D images therefore represent wetted two-grain boundaries.

[18] For sample SB8 with 1.6% melt, reconstruction of the 3-D melt geometry by software as described

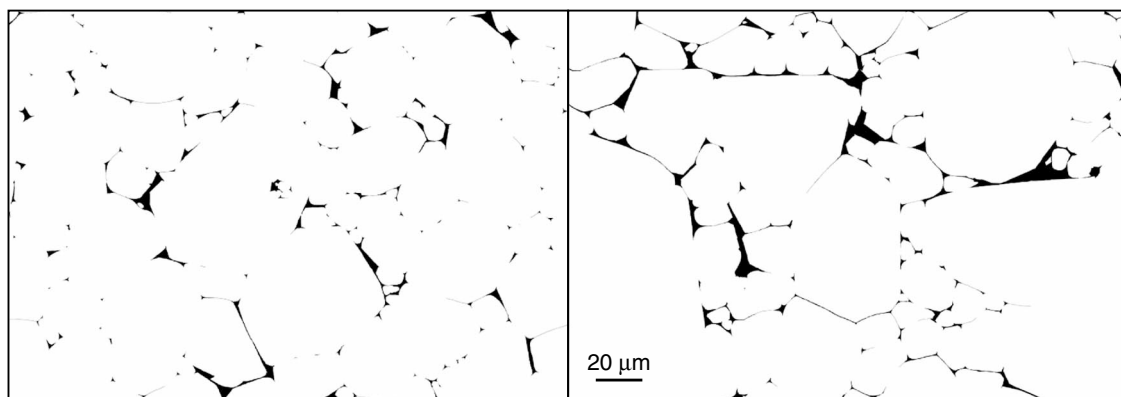


Figure 4. Binary images of a section of SB8 (left, 1.6% melt) and SB11 (right, 3.6% melt). The scale bar applies to both images. The images show a representative section of each sample. Melt pocket size and distribution are linked to the shape and size of the grains in the aggregate. The smallest pockets have the characteristic shapes of triple junction tubules. They occur at all three-grain edges, providing the backbone for interconnection and mobility of the melt. At 1.6% melt, larger pockets surrounded by four or more grains contain the bulk of the melt. At 3.6% melt, most of the melt is connected even in 2-D by layers wetting two-grain boundaries.

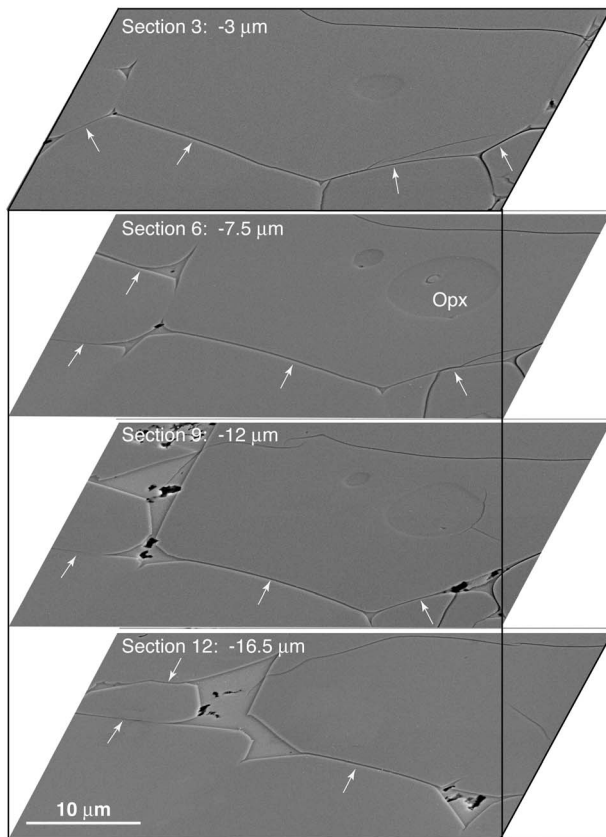


Figure 5. Images of the same area from four sections of sample SB11. The sections are separated by $\sim 4.5 \mu\text{m}$ each, for a total depth of $13.5 \mu\text{m}$. These images illustrate the persistence of melt layers (arrows) on two-grain boundaries with depth. By comparison, larger more irregularly shaped melt pockets at grain corners (left side of the images) change relatively rapidly with depth. Black areas within the melt pockets are graphite particles. The olivine grain in the center of the images grew around an orthopyroxene grain which can also be tracked with depth.

above was not satisfactory. Likely reasons are the small size of the triple junction tubules ($\sim 1 \mu\text{m}$ or less) relative to the spacing of the sections ($1.6 \mu\text{m}$), as well as offsets between sections of tubules that are inclined. In Figure 6, the sections are aligned and stacked without interpolation. In this view, triple junctions can be traced along grain edges over multiple sections with depth into the sample, but the view is dominated by larger pockets of melt. These pockets change shape from one section to the next, as also observed with relatively low-resolution serial sectioning [Wark *et al.*, 2003]. Wetted two-grain boundaries occur less frequently at this melt fraction. Overall, the melt is interconnected by the triple junction network, but a substantial portion of the volume of the melt resides in larger pockets.

[19] At 3.6% melt (sample SB11, Figure 7), the 3-D surfaces can be reconstructed as outlined in Section 2.4. The red surface represents crystal-melt interfaces, with crystalline grains removed. At this melt content, wetted grain boundaries are much more frequent, with some grains nearly completely surrounded by melt. The irregular appearance of some surfaces with depth is due to imperfect vertical alignment of the sections (Section 2.2).

4. Discussion

4.1. Dihedral Angles

[20] Image resolution is important not only for 3-D reconstruction of the melt geometry but also for measuring dihedral angles. The first dihedral angles in the system olivine and basaltic melt were measured on a light microscope [Waff and Bulau, 1979], with a reported value of 50° . Measurements on relatively low-magnification backscattered electron images resulted in a median angle of 49° [Toramaru and Fujii, 1986]. Daines and Kohlstedt [1993] reported dihedral angles of between 27 and 38° from SEM images of relatively fine-grained aggregates (mean grain size $< 10 \mu\text{m}$). Yoshino *et al.*, [2005] reported a dihedral angle of 34° , while [Yoshino *et al.*, 2009], using higher-resolution images reported a dihedral angle of 12° for a sample held at the same

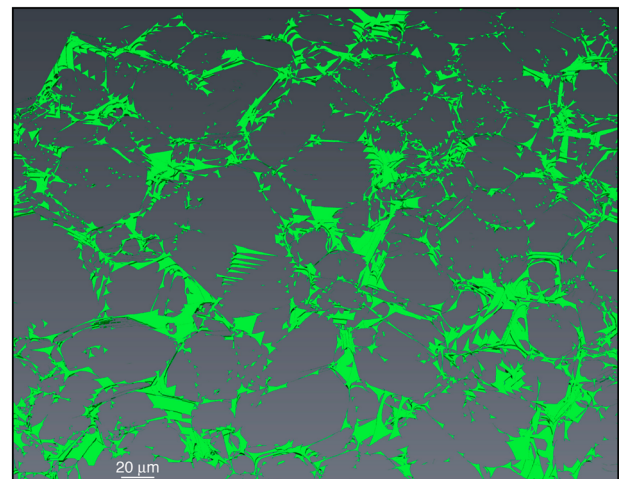


Figure 6. Inclined view of the stacked sections of sample SB8. Overall, at the grain size ($33 \mu\text{m}$) and melt fraction ($\sim 1.6\%$) of this sample, the melt geometry is dominated larger melt pockets which change relatively rapidly with depth and contain the bulk of the melt. The triple junction tubules constitute an interconnected network, but their size is small compared to the larger pockets. However, the triple junctions accommodate the flow of melt through the matrix at this melt fraction.

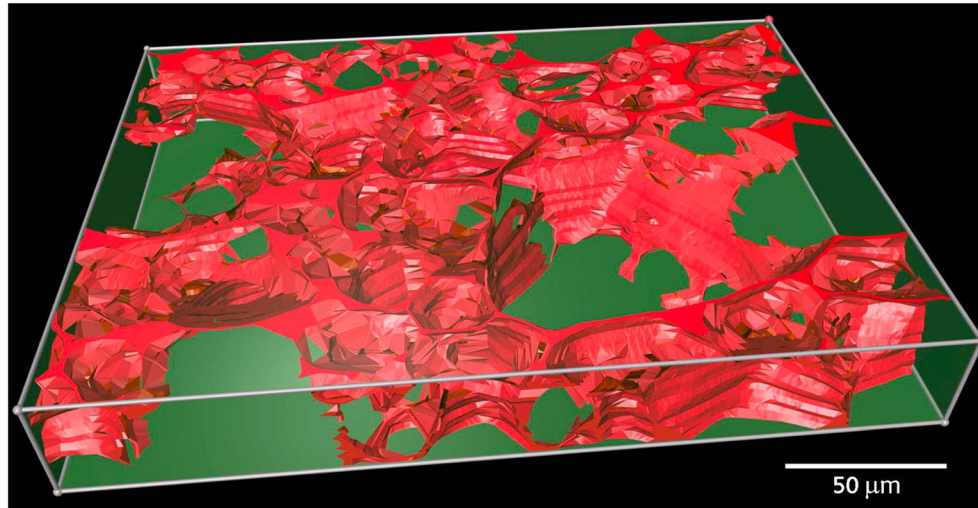


Figure 7. View from the top of the reconstructed 3-D melt distribution. Overall, at the grain size ($33\ \mu\text{m}$) and melt fraction ($\sim 3.6\%$) of this sample, the view of the 3-D melt geometry is dominated by wetted two-grain boundaries, with some smaller grains nearly completely surrounded by melt. The thin layers on two-grain boundaries seen in the 2-D images (Figure 2) persist in 3-D, confirming that they are sheet-like rather than a sectioning artifact of triple junction tubules.

temperature as our samples. This latter value agrees well with values of 10° from a TEM study *Cmíral et al.* [1998] and 12° reported in *Faul and Scott* [2006] from FE-SEM imaging. The study by *Cmíral et al.* [1998] also illustrates the effect of faceting on dihedral angles at the scale of tens of nm at low melt fractions.

[21] In the isotropic equilibrium model of surface energy-controlled melt distribution, wetted two-grain boundaries occur only for dihedral angles equal to zero. The resulting melt films are uniform in width for all grain boundaries, with a thickness that can be calculated from the force balance across the interfaces (e.g., 2 nm thick films for Si_3N_4) [*Clarke*, 1987]. In the olivine-basalt system examined here, some grain boundaries are wetted by melt (a dihedral angle of zero), but for others, the dihedral angle is greater than zero (a melt-free grain boundary to a resolution of 1 nm is shown for example in *Faul et al.* [2004, Figure 6]. The thickness of the melt layer wetting some of the grain boundaries is not uniform, and their number increases with melt fraction. These observations indicate that the melt distribution in this system cannot be explained by considering the surface tension balance at individual grain junctions in isolation from the aggregate as a whole.

4.2. Comparison with X-ray Tomography

[22] A synchrotron X-ray microtomography study was conducted by *Zhu et al.* [2011] to obtain 3-D

images of the melt geometry in experimentally produced samples of olivine with added basaltic melt. Due to the small contrast between silicate melt (glass) and olivine, they used an edge enhancement technique to help with the extraction of solid-melt interfaces. The reported resolution of $0.7\ \mu\text{m}$ means that smaller triple junctions and the layers on two-grain boundaries could not be resolved.

[23] The inability to resolve some of the triple junctions by X-ray microtomography is consistent with the connectivity analysis provided by *Zhu et al.* [2011]. In the ideal isotropic system, the connectivity of nodes (four-grain junctions) should be four, while the X-ray tomographic study found 50% single-connected nodes at their lowest melt content of 2%. These single-connected nodes are dead ends [*Zhu et al.*, 2011, Figures 2A and 3A]; i.e., they imply melt-free three-grain edges. With a further decrease in melt fraction, X-ray tomography would therefore predict loss of connectivity of the melt. In contrast, high-resolution TEM imaging of a sample with a melt fraction of $\sim 10^{-4}$ showed that all three-grain edges contain melt [*Faul et al.*, 2004].

[24] The importance of sufficient resolution is illustrated by a comparison of Figure 8a, showing a subset of the imaged volume of the sample SB11 at the resolution of this study, and Figure 8b where the same volume is eroded to a resolution comparable to the X-ray tomography (i.e., a voxel size of $0.7\ \mu\text{m}$). The erosion removes the layers on two-grain boundaries as well as some triple

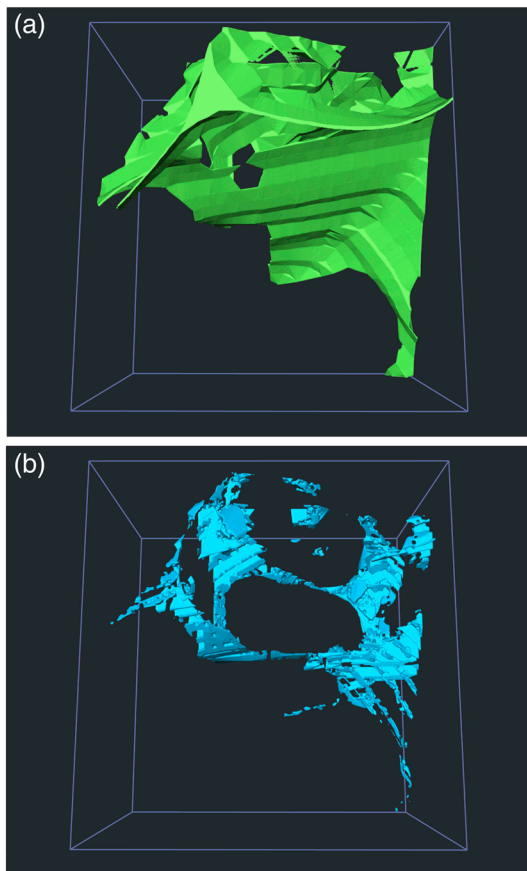


Figure 8. Detail of the 3-D pore space from the volume shown in Figure 7. (a) At the full resolution of this study, melt layers on grain boundaries and small triple junctions are present. The voxel size is $0.025 \mu\text{m}$. (b) The same volume as in Figure 8a sampled with a voxel size of $0.7 \mu\text{m}$, the resolution of the X-ray tomographic study [Zhu *et al.*, 2011]. The thin layers of melt are not captured at this resolution.

junctions. The resultant change in melt geometry and connectivity affects all physical properties of the partially molten rock. Another consideration is that, as stated by Zhu *et al.* [2011], the software used to determine the connectivity is not suitable for the analysis of sheets or layers.

4.3. Origin of Wetted Two-grain Boundaries

[25] Grain growth as well as the geometry of intergranular melt is the result of surface energy reduction. For both cases, the chemical potential μ is proportional to the ratio of surface tension γ and a radius of curvature, r , as $\mu \sim \gamma/r$. For grain growth, the radius in this equation is the mean grain size of the aggregate [Atkinson, 1988], while for establishment of the dihedral angle, r is the mean interfacial curvature of the abutting grain surfaces

[Waff and Bulau, 1979]. For both processes, occurring simultaneously in the same system and hence driven by the same surface tension, the chemical potential can be decreased by increasing r .

[26] During grain growth of a polycrystalline aggregate, grains below a certain radius shrink, while larger grains grow, resulting in a self-similar normalized grain size distribution [Faul and Scott, 2006]. Shrinking grains eventually disappear, requiring adjustment of the local grain surface geometry of their former neighbors. Consequently, the melt geometry is not fixed by static surface tension equilibrium between unchanging neighboring grains but is the result of a dynamic process responding to continually changing grain surfaces. This process is directly observable in a partially molten analogue system consisting of norcamphor and ethanol [Walte *et al.*, 2003]. These experiments show that even for a relatively isotropic system, wetted two-grain boundaries are a transient feature of continuing grain growth. However, while individual features are transient, the aggregate as a whole will always have a fraction of wetted two-grain boundaries as grain growth proceeds. For partially molten olivine, wetted two-grain boundaries are further stabilized by the small dihedral angle [Cmiral *et al.*, 1998; Faul and Scott, 2006], implying that the surface energy difference between a wetted and a melt-free two-grain boundary is small. Large pockets of melt are stabilized at the site of shrinking grains due to the establishment of slow-growing, faceted grain surfaces [Waff and Faul, 1992].

5. Implications

5.1. Seismic Properties

[27] Wetted two-grain boundaries significantly change the physical properties of partially molten rocks. Melt can affect seismic velocities and attenuation by a number of processes, among them melt “squirt,” the flow of melt between adjacent inclusions with different orientations relative to the applied stress [Mavko and Nur, 1975]. Depending on the aspect ratio (ratio of short to long axis) of the assumed ellipsoidal inclusions and the viscosity of the melt, this process can occur at seismic frequencies and hence cause attenuation due to melt [e.g., O’Connell and Budiansky, 1977]. Melt squirt should result in a peak in attenuation at the frequency at which squirt flow occurs.

[28] Aspect ratios determined from relatively low-resolution images in 2-D have a value around 0.05

when inclusions connected in 2-D images are analyzed as a whole [Faul *et al.*, 1994]. With these aspect ratios, based on the analysis of Schmeling [1985] [see also Hammond and Humphreys, 2000], melt squirt occurs at frequencies above those used in the experiments of Jackson *et al.* [2004] and Faul *et al.* [2004] and hence cannot be the cause for the experimentally observed attenuation peak. Instead, this peak was ascribed to elastically accommodated grain boundary sliding. However, a recent theoretical analysis of grain boundary sliding, utilizing somewhat relaxed geometric constraints relative to an earlier model [Raj and Ashby, 1971], similarly predicts that this process occurs at higher frequencies or lower temperatures [Morris and Jackson, 2009]. Correspondingly, the relatively mild plateau observed experimentally in melt-free samples moves out of the seismic frequency band to frequencies above 1 Hz at 900°C at a grain size of 3 μm [Jackson and Faul, 2010]. By contrast, the peak observed only for melt-bearing samples leaves the seismic frequency band at a temperature of about 1250°C at a grain size of 9 μm [Jackson *et al.*, 2004].

[29] Individual layers on two-grain boundaries have significantly lower aspect ratios than the combined inclusions that were examined by Faul *et al.* [1994]. At experimental grain sizes of $\sim 30 \mu\text{m}$, the aspect ratio for a 10–100 nm thick layer is of order of 10^{-3} to 10^{-4} . For this aspect ratio melt “squirt” is predicted to occur in the frequency range of the experiments, consistent with the experimental observations [Jackson *et al.*, 2004]. The correlation of peak height with melt fraction can be attributed to an increasing number of low aspect ratio inclusions with increasing melt fraction, as observed for the samples in this study.

[30] For a squirt-related attenuation peak to be in the seismic frequency range, aspect ratios of melt inclusions in the mantle have to be in a similar range as in the experiments. With estimated grain sizes from 1 mm to 1 cm, the layer thickness of wetted grain boundaries in the upper mantle needs to be in the range from 100 nm to 1 μm for observable melt-related attenuation at seismic frequencies. Measurement of the wetness for samples with similar melt content shows that the wetness increases with increasing grain size (Section 3). At mantle grain sizes in the range from mm to cm wetted grain boundaries may therefore occur more frequently at lower melt fractions relative to the experimental grain sizes. Further work is needed to quantify the relationship between grain size and wetness for constant melt content.

[31] Seismological studies of subduction zones find Q values that are too low to be explained by temperature alone (e.g., northeastern Japan [Takanami *et al.*, 2000] and Nicaragua and Costa Rica [Rychert *et al.*, 2008]). Back-arc regions tend to have lower Q than the arc itself, for example in the Lau Basin [Roth *et al.*, 1999; Wiens *et al.*, 2008], Marianas [Pozgay *et al.*, 2009], and the central Andes [Schurr *et al.*, 2003]. Since the lowest velocities and highest attenuation are observed beneath the back-arc rather than the arc (where the highest water contents are observed, e.g., Kelley *et al.* [2010]), it is likely that melt plays a significant role for the seismic properties. Melt-related attenuation precludes triple junction tubules as the cause since the attenuation peak occurs at higher frequencies, outside the seismic band [e.g., Schmeling, 1985; Takei, 2002].

5.2. Permeability

[32] The effect of the observed 3-D melt distribution on permeability is more difficult to estimate. Due to the limited resolution, X-ray microtomography substantially underestimates the connectivity of the melt at low melt fractions, but it does image larger conducting elements at high melt fractions. Consistent with previous 2-D observations [Faul *et al.*, 1994; Faul, 1997], the 3-D images show an increase in the number of wetted two-grain boundaries with increasing melt fraction. At low melt fractions, the sequestration of melt in larger pools reduces the permeability for this melt fraction relative to the isotropic equilibrium model, for which an increase in melt fraction is coupled to an increasing triple junction tubule diameter [e.g., Faul, 2001]. This permeability reduction due to the stabilization of larger melt pools by faceting was also recognized by Yoshino *et al.* [2006]. To quantify the evolution of permeability with melt fraction while taking the changing melt geometry into account requires numerical modeling of the observed 3-D pore geometry with for example the lattice-Boltzmann method [e.g., Ferreol and Rothman, 1995].

6. Conclusions

[33] Serial sectioning of experimentally produced partially molten samples with a steady state grain size distribution shows that wetted two-grain boundaries exist in aggregates with dihedral angles $>0^\circ$. These wetted grain boundaries are a dynamic feature due to grain growth, which, like the

formation of dihedral angles, is driven by surface energy reduction. The melt geometry in partially molten systems therefore cannot be characterized by dihedral angles alone. The grain boundary wetness, as defined by *Takei* [1998], may be more suitable for characterization of the melt distribution from 2-D images, provided they are of adequate resolution. Grain growth, driven by surface energy reduction, will also occur in the mantle, resulting in a similar normalized grain size distribution away from high-stress regions (see for example *Faul* [1997, Figure 1] for the grain size distribution of a xenolith).

[34] The 3-D melt distribution, obtained from serial sectioning and high-resolution imaging, confirms that the number of wetted grain boundaries increases with melt content, consistent with previous observations [*Faul et al.*, 1994; *Faul*, 1997]. Wetted two-grain boundaries were also noted under hydrous conditions at high pressure [*Yoshino et al.*, 2007] and at anhydrous conditions at high temperatures and pressures [*Yoshino et al.*, 2009]. Preliminary observations suggest that the number of wetted grain boundaries increases with increasing grain size at constant melt content. The wetted grain boundaries with their low aspect ratios (of order of 10^{-3} to 10^{-4}) can explain the experimental observations of an attenuation peak in partially molten samples that is absent in melt-free samples [*Jackson et al.*, 2004; *Faul et al.*, 2004]. Melt will therefore have a significant effect on both seismic velocities and attenuation as determined by these studies.

Acknowledgments

[35] Review of this manuscript by Takashi Yoshino and an anonymous reviewer is gratefully acknowledged. This work was supported by NSF grant EAR-0838447.

References

Atkinson, H. (1988), Theories of normal grain growth in pure single phase systems, *Acta Metall.*, *36*(3), 469–491.

Bulau, J. R., H. S. Waff, and J. A. Tyburczy (1979), Mechanical and thermodynamic constraints on fluid distribution in partial melts, *J. Geophys. Res.*, *84*, 6102–6108.

Clarke, D. R. (1987), On the equilibrium thickness of intergranular glass phases in ceramic materials, *J. Am. Ceram. Soc.*, *70*, 15–22.

Cmíral, M., J. D. Fitz Gerald, U. H. Faul, and D. H. Green (1998), A close look at dihedral angles and melt geometry in olivine-basalt aggregates: A tem study, *Contrib. Mineral. Petr.*, *130*, 336–345.

Daines, M. J., and D. L. Kohlstedt (1993), A laboratory study of melt migration, *Phil. Trans. Royal Soc. Lond.*, *342*, 43–52.

Edelsbrunner, H., and E. P. Mücke (1994), Three-dimensional alpha shapes, *ACM T. Graphic.*, *13*(1), 43–72.

Faul, U. H. (1997), Permeability of partially molten upper mantle rocks from experiments and percolation theory, *J. Geophys. Res.*, *102*, 10,299–10,311.

Faul, U. H. (2000), Constraints on the melt distribution in anisotropic polycrystalline aggregates undergoing grain growth, in *Physics and Chemistry of Partially Molten Rocks*, edited by N. Bagdassarov, D. Laporte, A. B. Thompson, pp. 67–92, Kluwer Academic Publishers, Dordrecht.

Faul, U. H. (2001), Melt retention and segregation beneath mid-ocean ridges, *Nature*, *410*, 920–923.

Faul, U. H., and D. Scott (2006), Grain growth in partially molten olivine aggregates, *Contrib. Mineral. Petr.*, *151*, 101–111, doi:10.1007/s00410-005-0048-1.

Faul, U. H., D. R. Toomey, and H. S. Waff (1994), Intergranular basaltic melt is distributed in thin, elongated inclusions, *Geophys. Res. Lett.*, *21*, 29–32.

Faul, U. H., J. D. Fitz Gerald, and I. Jackson (2004), Shear wave attenuation and dispersion in melt-bearing olivine polycrystals: 2. Microstructural interpretation and seismological implications, *J. Geophys. Res.*, *109*, B06,202, doi:10.1029/2003JB002,407.

Ferreol, B., and D. H. Rothman (1995), Lattice-Boltzmann simulations of flow through fontainebleau sandstone, *Transport Porous Med.*, *20*, 3–20.

Hammond, W., and E. D. Humphreys (2000), Upper mantle seismic wave attenuation: Effects of realistic partial melt distribution, *J. Geophys. Res.*, *105*, 10,987–10,999.

Herbert, L. B., and L. G. J. Montési (2010), Generation of permeability barriers during melt extraction at mid-ocean ridges, *Geochem. Geophys. Geosyst.*, *11*, Q12,008, doi:10.1029/2010GC003,270.

Hernlund, J. W., P. J. Tackley, and D. J. Stevenson (2008), Buoyant melting instabilities beneath extending lithosphere: 1. Numerical models, *J. Geophys. Res.*, *113*, B04,405, doi:10.1029/2006JB004,862.

Jackson, I., and U. H. Faul (2010), Grainsize-sensitive viscoelastic relaxation in olivine: Towards a robust laboratory-based model for seismological application, *Phys. Earth Planet. In.*, *183*, 151–163, doi:10.1016/j.pepi.2010.09.005.

Jackson, I., U. H. Faul, J. D. Fitz Gerald, and B. H. Tan (2004), Shear wave attenuation and dispersion in melt-bearing olivine polycrystals: 1. Specimen fabrication and mechanical testing, *J. Geophys. Res.*, *109*, B06,201, doi:10.1029/2003JB002,406.

Johnson, K. T. M., H. J. B. Dick, and N. Shimizu (1990), Melting in the oceanic upper mantle: An ion microprobe study of diop-sides in abyssal peridotites, *J. Geophys. Res.*, *95*, 2661–2678.

Katz, R. F. (2008), Magma dynamics with the enthalpy method: Benchmark solutions and magmatic focusing at mid-ocean ridges, *J. Petrol.*, *49*, 2099–2121, doi:10.1093/petrology/egn058.

Katz, R. F. (2010), Porosity-driven convection and asymmetry beneath mid-ocean ridges, *Geochem. Geophys. Geosyst.*, *11*, Q0AC07, doi:10.1029/2010GC003,282.

Kelley, K. A., T. Plank, S. Newman, E. M. Stolper, T. L. Grove, S. Parman, and E. H. Hauri (2010), Mantle melting as a function of water content beneath the mariana arc, *J. Petrol.*, *51*, 1711–1738, doi:10.1093/petrology/egq036.

Lamarre, P., C. Fulk, D. D’Orsogna, E. Bellotti, F. Smith, M. B. R. P. Lovecchio, T. Parodos, J. Marciniak, S. P. Tobin, and J. Markunas (2009), Characterization of dislocations in HgCdTe heteroepitaxial layers using a new substrate removal technique, *J. Electron. Mater.*, *38*, 1746–1754, doi:10.1007/s11664-009-0771-x.

- Mavko, G. M., and A. Nur (1975), Melt squirt in the asthenosphere, *J. Geophys. Res.*, *80*, 1444–1448.
- Morris, S., and I. Jackson (2009), Diffusionally-assisted grain-boundary sliding and viscoelasticity of polycrystals, *J. Mech. Phys. Solids*, *57*, 744–761, doi:10.1016/j.jmps.2008.12.006.
- O’Connell, R. J., and B. Budiansky (1977), Viscoelastic properties of fluid-saturated cracked solids, *J. Geophys. Res.*, *82*, 5719–5739.
- Pozgay, S. H., D. A. Wiens, J. A. Conder, H. Shiobara, and H. Sugioka (2009), Seismic attenuation tomography of the Mariana subduction system: Implications for thermal structure, volatile distribution, and slow spreading dynamics, GGG special issue *The Izu-Bonin-Mariana Subduction Factory: A Comprehensive Overview*, *10*, Q04X05, doi:10.1029/2008GC002,313.
- Raj, R., and M. F. Ashby (1971), On grain boundary sliding and diffusional creep, *Metall. Trans.*, *2*, 1113–1127.
- Roth, E. G., D. A. Wiens, L. M. Dorman, J. Hildebrand, and S. C. Webb (1999), Seismic attenuation tomography of the Tonga back-arc region using phase pair methods, *J. Geophys. Res.*, *104*, 4795–4809.
- Rychert, C. A., K. M. Fischer, G. A. Abers, T. Plank, E. Syracuse, J. M. Protti, V. Gonzalez, and W. Strauch (2008), Strong along-arc variations in attenuation in the mantle wedge beneath Costa Rica and Nicaragua, *Geochem. Geophys. Geosyst.*, *9*, Q10S10, doi:10.1029/2008GC002,040.
- Schmeling, H. (1985), Numerical models on the influence of partial melt on elastic, anelastic and electrical properties of rocks. Part 1: Elasticity and anelasticity, *Phys. Earth Planet. Int.*, *41*, 34–57.
- Schurr, B., G. Asch, A. Rietbrock, R. Trumbull, and C. Haberland (2003), Complex patterns of fluid and melt transport in the central Andean subduction zone revealed by attenuation tomography, *Earth Planet. Sci. Lett.*, *215*, 105–119, doi:10.1016/S0012-821X(03)00441-2.
- Simpson, G., M. Spiegelman, and M. I. Weinstein (2010), A multiscale model of partial melts: 2. Numerical results, *J. Geophys. Res.*, *115*, B04,411, doi:10.1029/2009JB006,376.
- Spiegelman, M., and P. Kenyon (1992), The requirements for chemical disequilibrium during magma migration, *Earth Planet. Sci. Lett.*, *109*, 611–620.
- Stracke, A., B. Bourdon, and D. McKenzie (2006), Melt extraction in the earth’s mantle: Constraints from U-Th-Pa-Ra studies in oceanic basalts, *Earth Planet. Sci. Lett.*, *244*, 97–112, doi:10.1016/j.epsl.2006.01.057.
- Takanami, T., I. S. Sacks, and A. Hasegawa (2000), Attenuation structure beneath the volcanic front in northeastern Japan from broad-band seismograms, *Phys. Earth Planet. Int.*, *121*, 339–357.
- Takei, Y. (1998), Constitutive mechanical relations of solid-liquid composites in terms of grain-boundary contiguity, *J. Geophys. Res.*, *103*, 18,183–18,203.
- Takei, Y. (2002), Effect of pore geometry on vp/vs: From equilibrium geometry to crack, *J. Geophys. Res.*, *107*, doi:10.1029/2001JB000,522.
- ten Grotenhuis, S. M., M. R. Drury, C. J. Spiers, and C. J. Peach (2005), Melt distribution in olivine rocks based on electrical conductivity measurements, *J. Geophys. Res.*, *110*, B12,201, doi:10.1029/2004JB003,462.
- Toramaru, A., and N. Fujii (1986), Connectivity of melt phase in a partially molten peridotite, *J. Geophys. Res.*, *91*, 9239–9252.
- Vaughan, P. J., D. L. Kohlstedt, and H. S. Waff (1982), Distribution of the glass phase in hot-pressed, olivine-basalt aggregates: An electron microscopy study, *Contrib. Mineral. Petr.*, *81*, 253–261.
- von Bargen, N., and H. S. Waff (1986), Permeabilities, interfacial areas and curvatures of partially molten systems: Results of numerical computations of equilibrium microstructures, *J. Geophys. Res.*, *91*, 9261–9276.
- Šrámek, O., Y. Ricard, and D. Bercovici (2007), Simultaneous melting and compaction in deformable two-phase media, *Geophys. J. Int.*, *168*, 964–982, doi:10.1111/j.1365–246X.2006.03,269.x.
- Waff, H., and J. R. Bulau (1979), Equilibrium fluid distribution in an ultramafic partial melt under hydrostatic stress conditions, *J. Geophys. Res.*, *84*, 6109–6114.
- Waff, H. S., and U. H. Faul (1992), Effects of crystalline anisotropy on fluid distribution in ultramafic partial melts, *J. Geophys. Res.*, *97*, 9003–9014.
- Walte, N. P., P. D. Bons, C. W. Passchier, and D. Koehn (2003), Disequilibrium melt distribution during static recrystallization, *Geology*, *31*, 1009–1012, doi:10.1130/G19815.1.
- Wark, D. A., C. A. Williams, E. B. Watson, and J. D. Price (2003), Reassessment of pore shapes in microstructurally equilibrated rocks, with implications for permeability of the upper mantle, *J. Geophys. Res.*, *108*, doi:10.1029/2001JB001,575.
- Watson, H. C., and J. J. Roberts (2011), Connectivity of core forming melts: Experimental constraints from electrical conductivity and x-ray tomography, *Phys. Earth Planet. Int.*, *186*, 172–182, doi:10.1016/j.pepi.2011.03.009.
- Wiens, D. A., J. A. Conder, and U. H. Faul (2008), The seismic structure and dynamics of the mantle wedge, *Ann. Rev. Earth Planet. Sci.*, *36*, 421–455, doi:10.1146/annurev.earth.33.092203.122633.
- Yoshino, T., Y. Takei, D. A. Wark, and E. B. Watson (2005), Grain boundary wetness of texturally equilibrated rocks, with implications for seismic properties of the upper mantle, *J. Geophys. Res.*, *110*, doi:10.1029/2004JB003,544.
- Yoshino, T., J. D. Price, D. A. Wark, and E. B. Watson (2006), Effect of faceting on pore geometry in texturally equilibrated rocks: Implications for low permeability at low porosity, *Contrib. Mineral. Petr.*, *152*, 169–186, doi:10.1007/s00,410–006–0099.
- Yoshino, T., Y. Nishihara, and S. i. Karato (2007), Complete wetting of olivine grain boundaries by a hydrous melt near the mantle transition zone, *Earth Planet. Sci. Lett.*, *256*, 466–472, doi:10.1016/j.epsl.2007.02.002.
- Yoshino, T., D. Yamazaki, and K. Mibe (2009), Well-wetted olivine grain boundaries in partially molten peridotite in the asthenosphere, *Earth Planet. Sci. Lett.*, *283*, 167–173, doi:10.1016/j.epsl.2009.04.007.
- Yoshino, T., M. Laumonier, E. McIsaac, and T. Katsura (2010), Electrical conductivity of basaltic and carbonatite melt-bearing peridotites at high pressures: Implications for melt distribution and melt fraction in the upper mantle, *Earth Planet. Sci. Lett.*, *295*, 593–602, doi:10.1016/j.epsl.2010.04.050.
- Zhu, W., G. A. Gaetani, F. Fusses, L. G. J. Montési, and F. D. Carlo (2011), Microtomography of partially molten rocks: Three-dimensional melt distribution in mantle peridotite, *Science*, *332*, 88–91, doi:10.1126/science.1202,221.